DFT-Based Quantum Mechanical and Molecular Docking Investigation of Synthesized Flavokawain B and Its Derivatives

[1]Saira Khan, [1]Muhammad Nadeem Akhtar*, [2]Seema Zareen, [1]Syeda Saba Hassan,
[3,4]Farhan Siddique, [4]Sumaira Nadeem, [1]Hijab Zainab and [1]Saima Riffat
[1]*Department of Chemistry, Faculty of Science, Ghazi University, Dera Ghazi Khan. Pakistan.*
[2]*Faculty of Industrial Sciences & Technology, University Malaysia Pahang,*
Lebuhraya Tun Razak 26300, Kuantan Pahang, Malaysia.
[3]*School of Pharmaceutical Science and Technology, Tianjin University,*
Tianjin 300072, P.R. China.
[4]*Department of Pharmaceutical Chemistry, Faculty of Pharmacy,*
Bahauddin Zakariya University, Multan 60800 Pakistan.
sumaira.6372@wum.edu.pk; nadeemupm@gmail.com

(Received on 22nd August 2024, accepted in revised form 17th December 2024)

Summary: Flavokawain B (FKB) is a naturally occurring chalcone that exhibits potential anti-cancer properties. Density functional theory (DFT) is a computational simulation approach used to investigate the electronic properties of molecules. Here, we investigated the structural-activity relationship and optoelectronic properties of naturally occurring chalcones; FKB and their derivatives named (*E*)-3’-(2’-fluorophenyl)-1’-(2’-hydroxy-4',6'-dimethoxyphenyl)prop-2-en-1-one (KG1), (*E*)-3'-(2'-chlorophenyl)-1'-(2-hydroxy-4',6'-dimethoxyphenyl)prop-2-en-1-one (KG2), (*E*)-3'-(4'-bromophenyl)-1'-(2'-hydroxy-4',6'-dimethoxyphenyl)prop-2-en-1-one (KG3), (*E*)-3'-(4'-fluorophenyl)-1'-(2'-hydroxy-4',6'-dimethoxyphenyl)prop-2-en-1-one (KG4), and (*E*)-1'-(2'-hydroxy-4',6'-dimethoxyphenyl)-3'-(3-nitrophenyl)prop-2-en-1-one (KG5) were used for computational approaches. The substituents in the acceptor moiety of derivatives were ortho F (KG1), ortho Cl (KG2), para Br (KG3), meta F (KG4), and meta nitro (KG5), respectively. The findings evaluated that the KG5 molecule showed excellent redshift (406 nm), the lowest excitation of 3.05 eV, lower HOMO of -6.25eV, LUMO of -2.82eV and a lower bandgap of 3.43eV. KG5 has a lower binding energy of 0.38eV, and electron mobility of 0.0206eV leading toward greater charge transference. The finding results showed that the presence of strong electron-withdrawing (KG5) on ring B in the FKB derivatives could make it an active site to attach the different types of proteins, which leads to becoming a potential bioactive compound. FKB and its derivatives were synthesized by our research group. These findings suggested that the KG5 molecule could be the best among all the derivatives and can be used for different biological assays.

Graphical Abstract

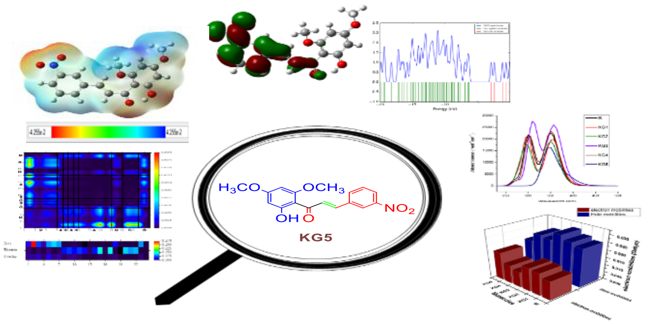

Keywords: Flavokawain B, Chalcone derivatives, DFT study, Optoelectronic properties, Energy bandgap.

Introduction

Flavokawain B (FKB) was extracted from the roots of *Piper methysticum* [1] and chosen as a reference compound (**R**) [2]. Chalcones have captured much interest from researchers looking for novel analogs of pharmacologically active substances [3, 4]. Chalcones and related analogs exhibited a variety of pharmacological effects, including antibacterial, antimalarial [5, 6], anticancer [7-9], antifungal [10], antioxidant [11, 12], and anti-inflammatory [13-15] properties. Chalcones are carbonyl compounds having unsaturated conjugated double bonds and consist of two rings with unsaturated carbonyl moiety. The FKB-type chalcone derivatives are synthesized by Claisen Schmidt condensation and previously reported its effects on breast cancerous cell lines [16-19] as shown in Fig. 1

***To whom all correspondence should be addressed.**

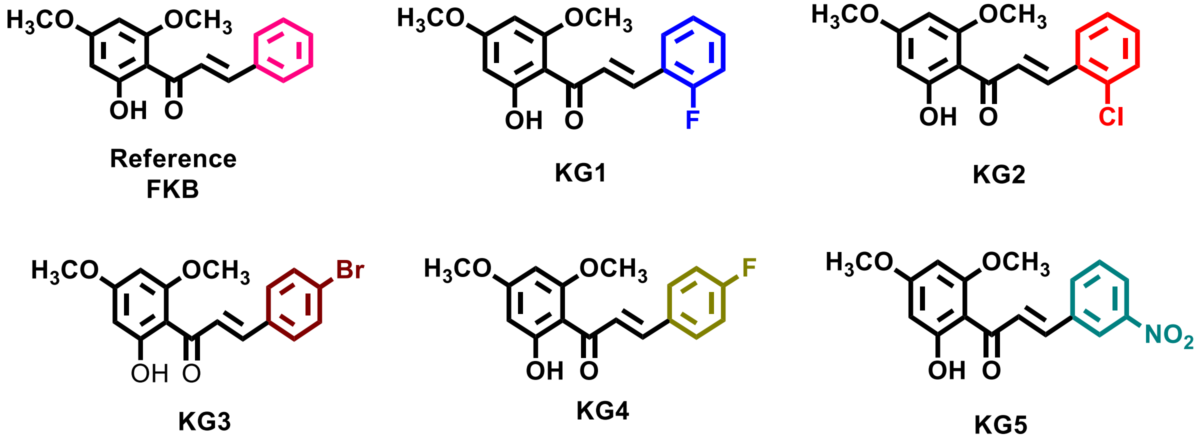

Fig. 1: Flavokawain B and its synthetic derivatives (KG1 to KG5).

The main objective of this analysis was to explore the optoelectronic characteristics of reference and all experimentally synthesized molecules (KG1-KG5) on a theoretical approach like DFT and (TF-DFT) theory. The four functionals were used to calculate the theoretical value of the reference to the parent compound. The different analyses were performed to determine binding energies, λ_{max}, bandgap values, TDM, PDOS plots, and electronic density distribution on HOMO/LUMO. Then, the findings revealed the most prominent drug among derivatives.

Computation Methodology

In this report, quantum mechanical simulations and molecules' geometrical optimization were performed by Gaussian09 [20]. For the visualization of molecular geometries, setting up input files, and displaying the computational outputs, Gauss View 5.0 was used [21]. For the validation of the method, the reference molecule was optimized at four different functionals named B3LYP, ωB97XD, CAM-B3LYP, and MPW1PW91 along with basis set 6-311G (d, p) [22]. Among all, B3LYP proved to be the best functional for calculations. The UV/Visible absorption graph of each modeled molecule in the gaseous state as well as in methanol solvent was obtained by using DFT. A conductor polarizable continuum model (CPCM) was used for calculations when a solvent is present [23]. Overlapping graphs, molecular electrostatic potential plots, transition density analysis, and density of states (DOS) were studied for all FKB derivatives. For plotting the absorption profiles, Origin 8.5 was utilized [23].

The reorganization energy plays a key role in this inquiry because charge mobilities are ominously influenced by this. There are two types of reorganization energies; internal and external. Internal reorganization energy addresses the alteration in a molecule's interior geometry. Variations in the external environment are associated with external factors. Here, calculations are related to internal reorganization energy because the current effort focuses on the alteration of internal structure. The following equations were used to calculate the mobility values for holes and electrons [24].

$$\lambda_h = [E_0^+ - E_+] + [E_+^0 - E_0] \text{ (Eq. 1)}$$
$$\lambda_e = [E_0^- - E_-] + [E_-^0 - E_0] \text{ (Eq. 2)}$$

The anionic, and cationic energies (E_0^- and E_0^+) also be determined by utilizing the above equation (1) and (2). Optimized cationic and anionic energies are shown by E_+ and E_-. Here, E_+^0 and E_-^0 represent the single point energies obtained from optimized geometries of cation and, anions correspondingly. E_0 symbolizes the single point energy (SPE) of a neutral molecule [25].

Glide Molecular Docking Methodology

Selection of target proteins

The crystal structures of the anti-inflammatory, anticancer, and antioxidant target proteins of interest (PDB ID: 4COX) [26], (PDB ID: 2WQN) [27], and (PDB ID: 5M8Q) [28], were fetched from the RCSB protein data bank (https://www.rcsb.org/) [29].

Pre-processing of target protein structures

The Protein Preparation Wizard module of the Maestro platform was employed to prepare the protein structures [30]. The module allocated jobs to prepare bond orders, add hydrogen atoms, make zero-order bonds to metals, create di-sulfate bonds, change the seleno-methionines into methionine, and fill up the missing side chains. The structures were then optimized by energy minimization and hydrogen bond optimization under the OPLS4 force field [31]. The LigPrep module of the Maestro platform was designated job to prepare the reference and the ligands (KG1, KG2, KG3, KG4, and

KG5), including the co-crystallized ligands of associated target proteins, each of them was prepared by BIOVIA [32].

Pre-processing of ligand structures

Three-dimensional structure of the R and its derivatives named KG1, KG2, KG3, KG4, and KG5 were prepared in Chem Draw 20.1.1 followed by their energy minimization via Chem3D 20.1.1 [33] and finally saved as the SDF file format. The LigPrep module of the Maestro platform was assigned the job of preparing all the ligands.

Glide Docking

The Maestro platform's Glide docking module executed the docking of the target proteins and ligand molecules [34]. The SP pose viewer analyzed the docked ligand and protein interactions and generated the optimal pose. The ligand interaction module created a 2D interaction diagram of the ligand-protein complex molecule, which was further visualized to explore the interaction between the ligand molecules and the target proteins during the binding process through the resulting SP posture.

Results and Discussions

In this study, computational studies were performed on synthesized FKB-type chalcone named (E)-1-(2-hydroxy-4,6-dimethoxyphenyl)-3-phenylprop-2-en-1-one used as isolated from *P. methysticum* roots known potential cytotoxic properties against cancer cells lines [2]. The alterations were done in ring B for the fabrication of FKB derivatives to study their optoelectronic and photovoltaic properties. For the initial optimization of the reference molecule, the diverse functionals B3LYP [35], ωB97XD [36], CAM-B3LYP [37], and MPW1PW91 [38] coupled with the basis set 6-311G (d, p) [39]. The B3LYP/6-311G (d, p) level [39] has been chosen for KG1-KG5 molecules because the reported experimental value of λ_{max} is 372 nm was the best match as opposed to the theoretical λ_{max} value of about 373 nm at this functional. Because of this, it supports subsequent simulations. Fig. 2. represents the theoretical λ_{max} of **R** attained at four functional mentioned as 373, 363, 319, and 318 nm, respectively. The UV absorption calculation showed that the R at B3LYP, CAM-B3LYP, MPW1PW91, and ωB97XD using the 6-31G (d, p) basis set of theory. The theoretical λ_{max} values for reference molecule obtained at all above-stated functionals were 375, 317, 360, and 316 nm, respectively.

(a) By using 6-311G (d,p)

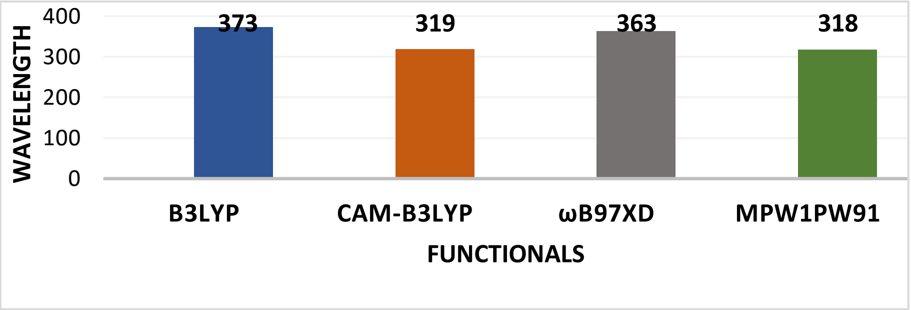

(b) By using 6-31G (d,p)

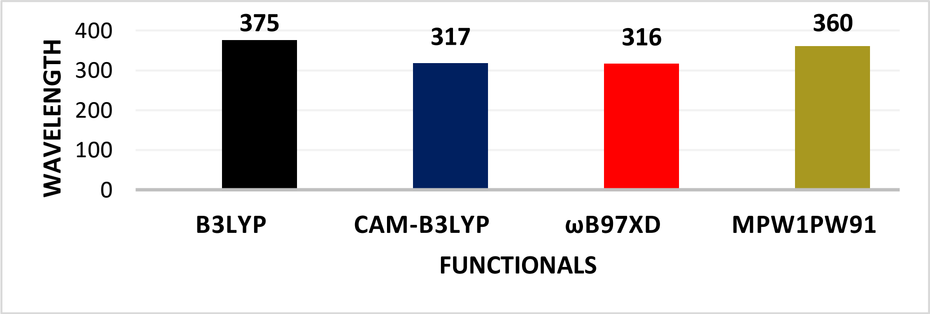

Fig. 2: (a) Comparison of the λ_{max} values of R at four functional along with 6-311G (d,p). (b) Comparison of the λ_{max} values of R at four functional along with 6-31G (d, p).

Frontier molecular orbital analysis.

For the evaluation of optoelectronic characteristics of all molecules, frontier molecular orbital analysis is a noteworthy parameter. At the B3LYP level coupled with a 6-311G (d, p) basis set, the FMO analysis on R and all selected derivatives KG1, KG2, KG3, KG4, and KG5 were carried out. Fig. 3. displayed the optimal geometries of FKB-type derivatives and reference molecules computed at density functional theory. Through a distribution scheme of frontier molecular orbitals, the photovoltaic characteristics and conductivities of all the molecules are inspected. The highest occupied molecular orbital is considered as HOMO or conduction band while the lowest unoccupied molecular orbital is considered as LUMO or valence band [40-43]. HOMO/LUMO energy difference gives energy band gap of reference and all FKB type derivatives. Furthermore, the excitation of electrons plays a crucial influence in the stabilization and de-stabilization of HOMO/LUMO [44]. As stability and electronic excitation have opposing relations, it implies that significantly destabilized HOMO may be obtained from higher electronic excitation [44]. Table-1**.** Showed the energy-gap, HOMO, and LUMO values of R and its derivatives (KG1-KG5). These computational studies were performed by calculating the following equation;

$$E_g = E_{HOMO} - E_{LUMO} \quad \text{(Eq. 3)}$$

The HOMO/LUMO band differences of R and FKB derivatives (KG1–KG5) are 3.96, 3.88, 3.91, 3.88, 3.96, and 3.43 eV, respectively. The declining sequence of HOMO for R and all observed molecules is listed as KG1>R>KG2>KG4>KG3>KG5. The dwindling sequence of LUMO for R and all observed molecules is R>KG4>KG1>KG2>KG3>KG5. The energy band gap ascending order of R and all fabricated molecules is given as KG5<KG3<KG1<KG2<KG4<R. Fig. 3. demonstrates the optimized geometries of R and its derivatives (KG1-KG5).

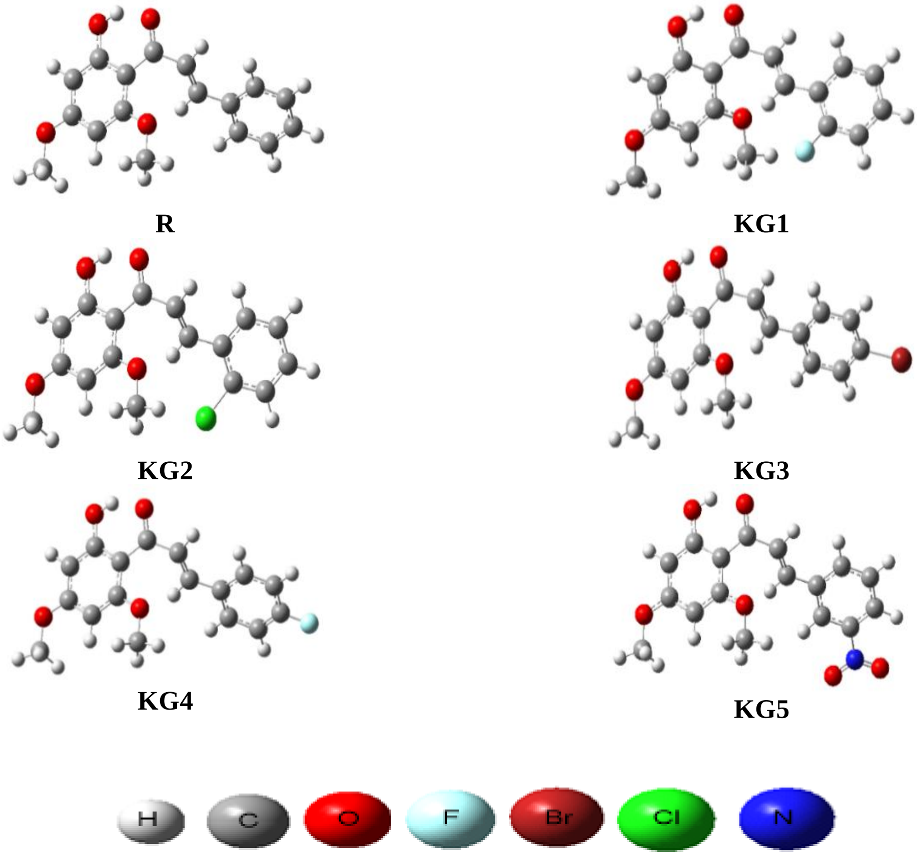

R **KG1**

KG2 **KG3**

KG4 **KG5**

Fig. 3: Illustration of the optimized reference molecule and KG1-KG5 molecules.

The electronic density distribution over HOMO and LUMO of the molecules are portrayed in Fig. 4. It is clearly shown in outcomes obtained from FMO analysis that there is uniformity in electronic density distribution around Ring A acting as donor moiety in HOMO of all molecules. In LUMO, electronic density distribution is frequently distributed throughout the molecule with maximal density on the acceptor and terminal units. So, the charge transferring will take place from donor to acceptor moiety throughout the molecule. The outcomes displayed that among all experimentally fabricated structures, the KG5 molecule showed the least HOMO, LUMO, and energy bandgap values due to the existence of nitro group present in the acceptor moiety. The Nitro group shows resonance phenomena along with extended conjugation that will lead to better efficiency of the molecule.

This study was also supported by the docking property of FKB and its derivatives [2, 45]. Firm connections inside the active site of Janus kinase were performed by docking [46]. The main purpose of docking was to see the active site for binding, stability, efficacy, and activity of the compound. According to findings, the KG5 molecule can provide a stable and good active site along with the protein because of the presence of the electron-withdrawing inductive group.

Table-1: Illustration of HOMO, LUMO, and energy bandgap values of R and all experimentally fabricated molecules.

Molecules	E_{HOMO} (eV)	E_{LUMO} (eV)	E_{gap} (eV)
R	-6.06402	-2.09952	3.96
KG1	-6.05613	-2.16864	3.88
KG2	-6.08388	-2.17353	3.91
KG3	-6.15545	-2.27503	3.88
KG4	-6.11626	-2.15503	3.96
KG5	-6.25667	-2.82168	3.43

Density of States.

Another crucial factor in determining the energy states contributing to occupied and unoccupied orbital is the density of the state [47, 48]. DOS is a graph representing how many states are in a molecule material per unit of energy as a function of energy. Although, it is frequently employed for vibrational mode and electronic states. DOS plots elucidate the allowed energy hypothetically for the transition when electrons show mobility from the valence band (occupied orbital) to the conduction band (unoccupied orbital). The gap between VB and CB indicates an energy band gap [49-51]. Using the 6-311G (d, p) basis set along with B3LYP functional, R, and all synthesized molecules (KG1-KG5), DOS analysis verified the FMO analysis.

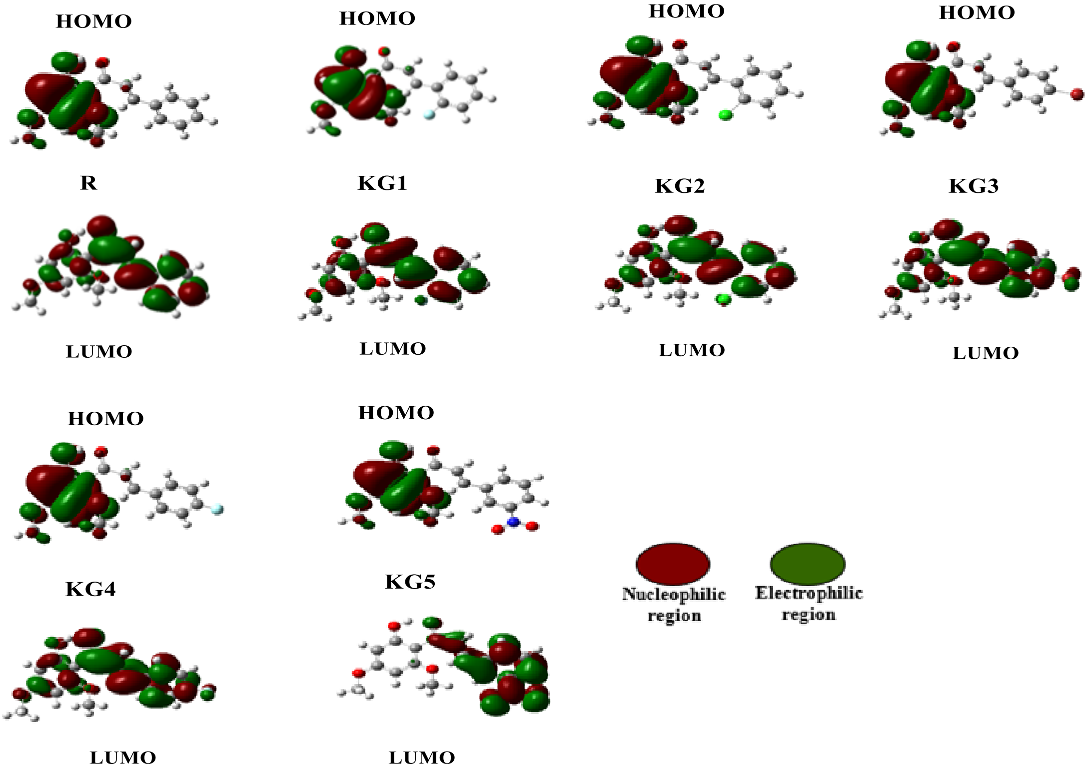

Fig. 4: Displaying optimized reference molecule and KG1-KG5 molecule.

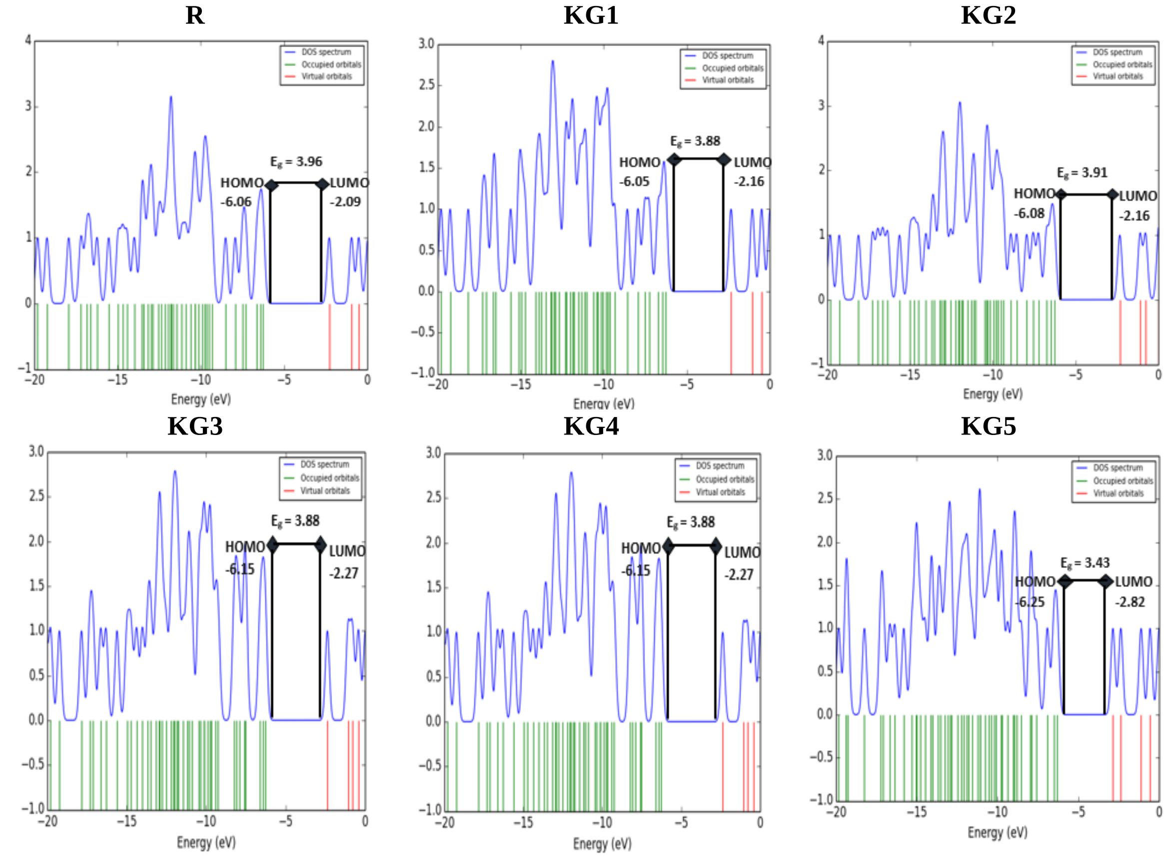
R **KG1** **KG2** **KG3** **KG4** **KG5**

Fig. 5: The density of states graphs for R and KG1-KG5 molecules simulated at B3LYP functional.

Two fragments make up the DOS graph. HOMO and LUMO represent the left and right sides of the plot respectively. While the energy band gap indicates the space between HOMO and LUMO where there are no electronic states. The overlapping of orbitals and distribution patterns across the molecule are observed on the DOS graph.

The findings demonstrated that R and all theoretically generated molecules had the same electronic density distribution pattern with a slight change in the HOMO region as shown in Fig. 5. It primarily lies over the Ring A but just marginally over π-bridge. The electronic density is, however, majorly distributed in the LUMO region of Ring B. The order of the DOS plots for R and all molecules is shown below;

KG5>KG3>KG4>KG2>R>KG1

The outcomes displayed that the KG5 molecule indicates a higher density of states in the LUMO region as compared to others due to the presence of the nitro group in Ring B. The nitro group is electro withdrawing leading towards extended conjugation.

Molecular Electrostatic Potential.

For the evaluation of a three-dimensional electronic charge distribution surface map is analyzed also known as molecular electrostatic potential (MEP) [22, 52]. Through this analysis, we can locate the electron-rich and poor sites over the molecule. The plots shown in Fig. 6. also suggest accessing the interaction of atoms within molecules. The color scale is given that depicts positive electrostatic potential and negative electrostatic potential. Negative extreme is represented by red and positive extreme is denoted by blue colour. The electron-rich centers are the carbonyl center and hydroxyl group.

Optical properties.

For the evaluation of UV-visible absorption spectra in methanol solvent by using a conductor-like polarizable continuum model, R, and all FKB derivatives are simulated at B3LYP level combined with 6-311G (d, p). Various optical characteristics like excitation energy, oscillator strength, absorption maxima (λ_{max}), dipole moment, about MO assignment are evaluated by using the DFT methodology [53-55]. The results obtained in the solvent phase are summarized in Table-2.

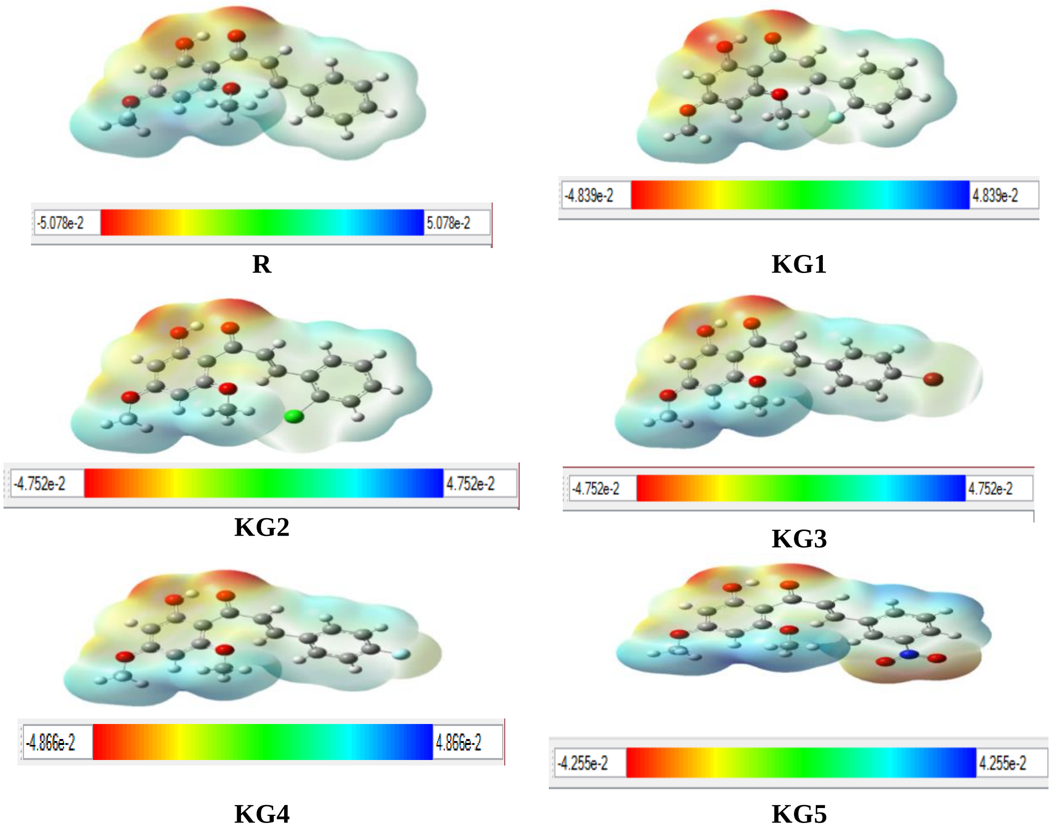

R **KG1**

KG2 **KG3**

KG4 **KG5**

Fig. 6: Representation of MEP graphs for all molecules calculated at B3LYP functional.

Table-2: Summarize the outcomes of optical properties like absorption maxima, excitation energy, and Dipole moment in solvent phase.

Molecules	Calculated λ_{max} (nm)	Exc. (eV)	Orc. Strength(f)	Assignment	Dipole moment
R	373	3.317	0.0542	HOMO->LUMO (98%)	9.1661
KG1	377	3.285	0.0434	HOMO->LUMO (98%)	8.5152
KG2	375	3.305	0.0366	HOMO->LUMO (98%)	7.8011
KG3	380	3.258	0.0577	HOMO->LUMO (98%)	8.2297
KG4	373	3.322	0.0588	HOMO->LUMO (98%)	8.4260
KG5	406	3.051	0.0081	HOMO->LUMO (98%)	5.6752

The findings showed that the experimentally obtained λ_{max} reported at 372 nm exhibits reasonable agreement with the DFT-based λ_{max} value of R calculated at 673 nm. The results demonstrated that changing the end-capped groups on the Ring B of the FKB molecule has a significant impact on absorption maximum spectra. All compounds (KG1–KG5) showed maximum values of absorption in the range of 373 and 406 nm. The UV region of the absorption spectra of all experimentally fabricated molecules (KG1–KG5) showed a red shift that is caused by the effective electron-withdrawing substituents present in the acceptor region of molecules. Bathochromic shift enhances the optoelectronic features of the molecule. Due to the presence of nitro group and prolonged extended conjugation, the KG5 molecule displayed maximum absorbance maxima among all. The endcap group also contributes to energy bandgap narrowing. For all modified molecules and R, the decreasing sequence of λ_{max} is KG5>KG3>KG1>KG2>R>KG4

Excitation energy is a significant factor that has been seen in Table-3. to see the impact. It is the quantity of energy required to raise the electrons from their resting state (ground) to their excited state. It is inversely related to the effectiveness of the molecule. Energy will be lower, and the efficiency of molecules will be higher [56-59]. The occurrence of effective acceptor moieties results in poor excitation energy for the molecules. The tabularized data showed that all FKB derivatives except KG4 have excitation energies less than R, which may be advantageous for effective charge transference. KG5 had the lowest excitation energy (3.05), resulting in excellent efficiency. The order of excitation energy increases as follows: KG5<KG3<KG1<KG2<R<KG4.

Another crucial factor is oscillator strength, which expresses molecular absorption and emission as a change in energy state. Higher light-harvesting energy is caused by stronger oscillators. Major molecular orbital assignments, which represent the transitions between HOMO and LUMO, are the next element discussed here. All the molecules except KG5 demonstrated a contribution of around 98% relative to the R molecule.

Table-3. summarizes the results of optical properties in gaseous state. The decreasing sequence of absorption maxima values for the R and all experimentally formed molecules is listed as KG5>KG1>KG3>KG2>KG4>R. It is suggested from the optical properties that the KG5 molecule showed the best results among all due to its high λ_{max} value, and small excitation energy. The UV graph of all molecules in both phases is depicted in Fig. 7.

Table-3: Summarize the outcomes of absorption maxima, excitation energy, and Dipole moment in the gaseous phase.

Molecules	Calculated λ_{max} (nm)	Exc. (eV)	Osc. Strength (*f*)	Assignment	Dipole moment (Debye)
R	**371**	**3.334**	**0.0159**	**HOMO->LUMO (98%)**	**6.8124**
KG1	**380**	**3.262**	**0.0137**	**HOMO->LUMO (98%)**	**6.3231**
KG2	**377**	**3.286**	**0.0137**	**HOMO->LUMO (98%)**	**5.7919**
KG3	**379**	**3.263**	**0.0153**	**HOMO->LUMO (98%)**	**6.1315**
KG4	**372**	**3.330**	**0.0158**	**HOMO->LUMO (98%)**	**6.2365**
KG5	**410**	**3.022**	**0.0038**	**HOMO->LUMO (98%)**	**4.3044**

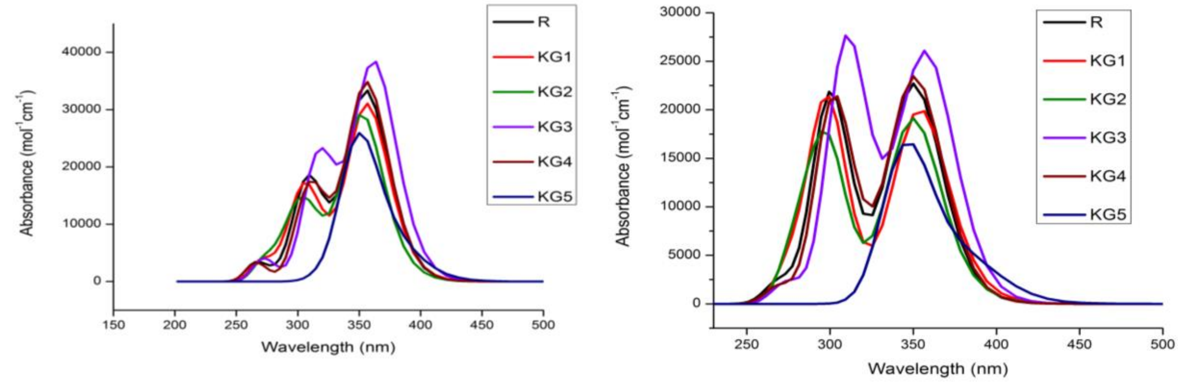

Fig. 7: Demonstration of UV graph of all molecules in solvent and gaseous phase.

Dipole moment.

To see the polarity of all experimentally synthesized molecules (KG1-KG5), another revealing factor is dipole moment analysis. The solubility of a molecule in a polar solvent is directly proportional to the dipole moment. It means highly polar solvent increases the solubility of drugs having larger dipole moments [60]. The dipole moment influences how charge moves between HOMO and LUMO in experimentally synthesized molecules; the greater the dipole moment, the faster will be electron transference within the molecule. When molecules get excited, their polarity increases. However, this only lasts for a short time before de-excitation occurs.

Table-4: Summarizes the outcomes of Dipole moment obtained in solvent and gaseous phase.

Molecules	μ_s (Debye)	μ_g (Debye)	μ_s - μ_g (Debye)
R	**9.1661**	**6.8124**	**2.3537**
KG1	**8.5152**	**6.3132**	**2.2020**
KG2	**7.8011**	**5.7919**	**2.0092**
KG3	**8.2297**	**6.1315**	**2.0982**
KG4	**8.4260**	**6.2365**	**2.1895**
KG5	**5.6752**	**4.3044**	**1.3708**

The dipole moment was simulated at B3LYP/6-311G (d, p) in the presence of methanol used as a solvent utilizing the CPCM model. Table 4. lists the simulated strength of the dipole moment of every molecule. The findings suggest that in the methanol solvent, the predicted dipole moment strength is higher, while in the gaseous phase, it is lower. This enhancement in dipole is due to the interaction of the solvent molecule with the fabricated molecule. While this type of interaction is missing in the gaseous phase. All the molecules showed comparable results concerning the reference molecule. In the solvent phase and gaseous state, the order of dipole moment of all molecules and R is the same given as R>KG1>KG4>KG3>KG2>KG5

Reorganization energy.

To see the effectiveness of a drug, another crucial approach is the reorganization of energy [22, 61, 62]. Electron and hole mobilities are correlated with reorganization energy in a contrary relation. It means that the lower reorganization energy of the molecule offers higher electron and hole mobilities.

There are two types of reorganization energy internal and external energy. However, in this study, we are focusing only on internal reorganization energy.

In the present work, we calculated the reorganization energy values for holes and electrons utilizing the B3LYP/ 6-311 G (d, p) technique of DFT. Table 5. represents the electron and hole reorganization energies for all molecules. Similarly, the reorganization graph for R and all modeled molecules are demonstrated in Fig. 8. The electron mobility for R is 0.0256 D while the electron mobilities for KG1, KG2, KG3, KG3, KG4, KG5 are 0.0275, 0.0302, 0.0251, 0.0261, and 0.0206 D correspondingly. The findings showed excellent insight into boosting electron mobilities of KG1, KG2, and KG3 molecules. Among all KG5 molecules demonstrated the lowest reorganization energy value due to higher charge transference between donor and electron-deficient acceptor moiety. The decreasing sequence for all molecules for electron mobility is; KG2>KG1>KG4>R>KG3>KG5.

On the other hand, the theoretically obtained hole mobility value for the R molecule is 0.0125 D. While the hole mobilities for KG1, KG2, KG3, KG3, KG4, KG5 are 0.0150, 0.0156, 0.0103, 0.0122, and 0.0185 D, respectively. It is suggested from the finding that hole mobilities of KG3, and KG4 vibrant molecules are the lowest showing higher charge transfer. The descending order for hole mobilities is; KG5>KG2>KG1>R>KG4>KG3. So, the molecules showed comparable reorganization energy values for electrons and holes in comparison to the R.

Table-5: Theoretically calculated Holes and Electron mobility values for all molecules.

Molecules	λ_e **(eV)** [a]	λ_h **(eV)** [b]
R	**0.0256**	**0.0125**
KG1	**0.0275**	**0.0150**
KG2	**0.0302**	**0.0156**
KG3	**0.0251**	**0.0103**
KG4	**0.0261**	**0.0122**
KG5	**0.0206**	**0.0185**

[a]Reorganizational energy of electron [b] Reorganizational energy of hole

Transition Density Matrix and Binding Energy.

For the calculation of the charge transfer of electrons in an excited state, another prominent tool is the transition density matrix (TDM). It facilitates the electronic excitation dynamics, and hole-electron localization/delocalization when they are excited. TDM also helps to observe the interaction between D/A [63-65].

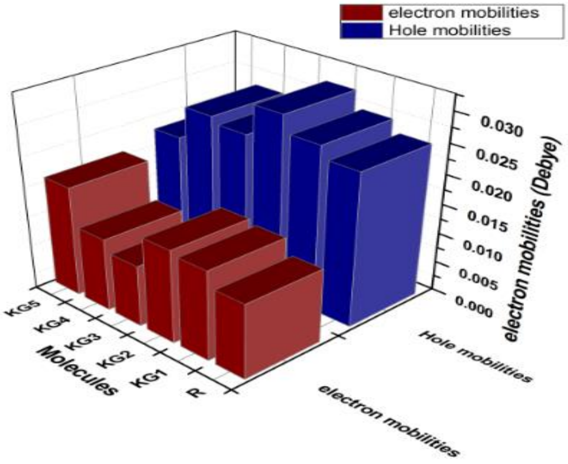

Fig. 8: Reorganization energy graphs for all fabricated molecules.

By doing simulations on the reference molecule and KG1-KG5 by utilization of B3LYP/6-311G (d, p) in an excited state, TDM plots are obtained. The graphs are depicted in Fig. 9. Hydrogen atoms have no transition; hence their impact is omitted. The TDM plot consists of three fragments; Donor, acceptor, and π-bridge. This heat map plot demonstrated the diagonal relationship between donor and acceptor via π-bridge.

The graph showed that the KG5 molecule has greater electron coherence in the acceptor region due to the presence of the nitro group. It facilitates greater charge transfer and the simplest dissociation of exciton in the S_0-S_1. The decreasing order for all molecule is given as KG5>KG3>KG4>KG2>KG1>R.

Another important factor to evaluate the charge separation efficiency of the compound is binding energy. Binding energy can be defined as the amount of energy required to dissociate the columbic forces holding exciton [66]. An exciton is an electron-hole pair bounded by forces [67]. When light is absorbed by a compound, the electron gets excited from HOMO to LUMO. The hole is generated in the HOMO of the donor moiety. The binding energy should be needed to dissociate it. It is denoted by “E_g”. For efficient charge separation, binding energy must be low. The binding energy can be computed by using the formula given below;

$$E_b = E_{L-H} - E_{opt} \quad \text{(iv)}$$

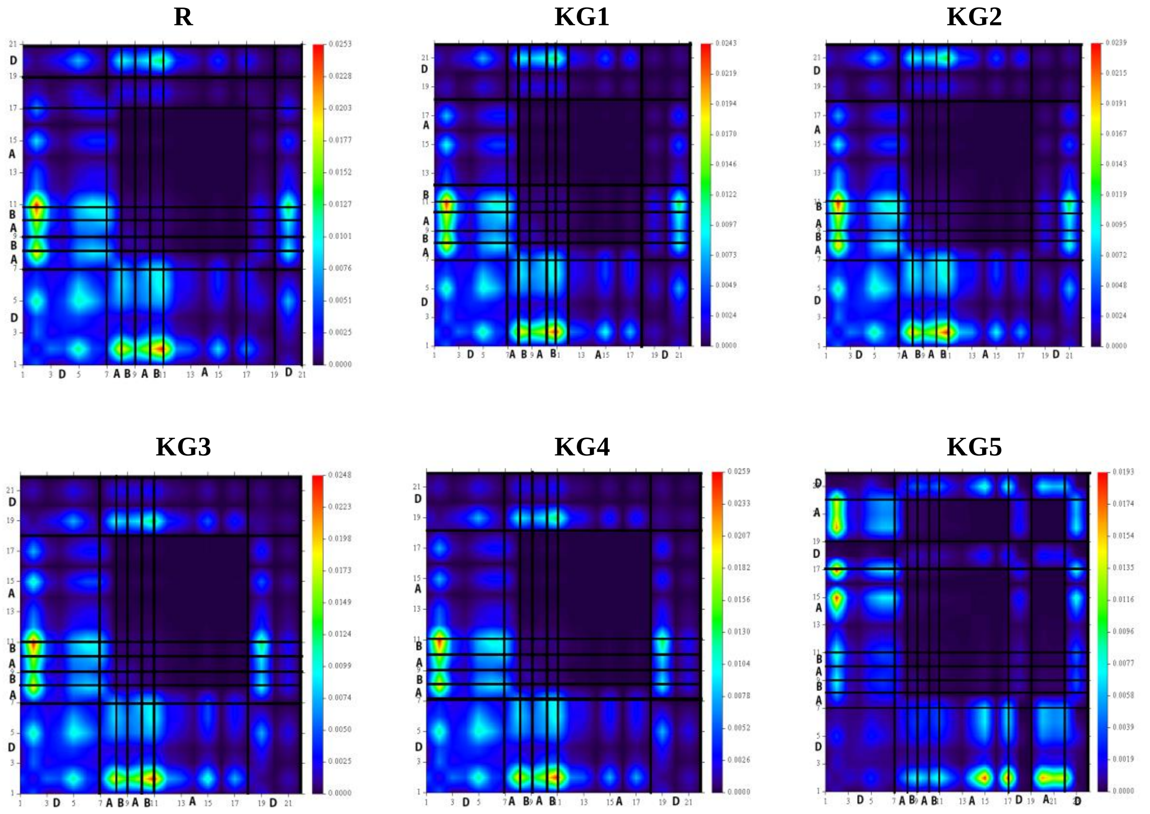
R
KG1
KG2
KG3
KG4
KG5

Fig. 9: Depiction of TDM plots for R and all fabricated molecules at the B3LYP level.

The HOMO/LUMO bandgap is exhibited by E_{L-H} [68]. E_{opt} however, stands for the minimal energy required for the first excitation [69, 70]. The binding energy of the reference molecule and all FKB derivatives were simulated on B3LYP combined with 6-311G (d, p). The theoretical values of binding energy for all molecules are summarized in Table 6. The findings demonstrated that all molecules have lower binding energies as compared to reference molecules. It means all molecules are efficient. The reference molecule has E_g value of 0.64eV. Among them, the KG5 molecule exhibited the lowest E_g of about 0.38eV. The molecules having somewhat higher E_b values are due to the localization, which reinforces the columbic forces of attraction between holes and electrons.

All experimentally synthesized molecules and R have decreasing binding energy values in the following sequence: R>KG4>KG3>KG2=KG1>KG5. The findings of the TDM heat map are further supported by electron-hole overlapping plots shown in Fig. 10.

Table-6: Calculated binding energy values for all molecules using the DFT approach.

Molecules	**E_{H-L} (eV)**	**E_{opt} (eV)**	**E_b (eV)**
R	**3.96**	**3.31**	**0.64**
KG1	**3.88**	**3.28**	**0.60**
KG2	**3.91**	**3.30**	**0.60**
KG3	**3.88**	**3.25**	**0.62**
KG4	**3.96**	**3.32**	**0.63**
KG5	**3.43**	**3.05**	**0.38**

This overlapping graph represents the contribution of electrons and holes. Non-hydrogen atoms are displayed in the x-axis. While different hues show the overlapping of holes and electrons according to their corresponding contributions. The major overlapping contribution is displayed by red color. According to the findings, KG5 had the maximum contribution in both hole and electron among all molecules.

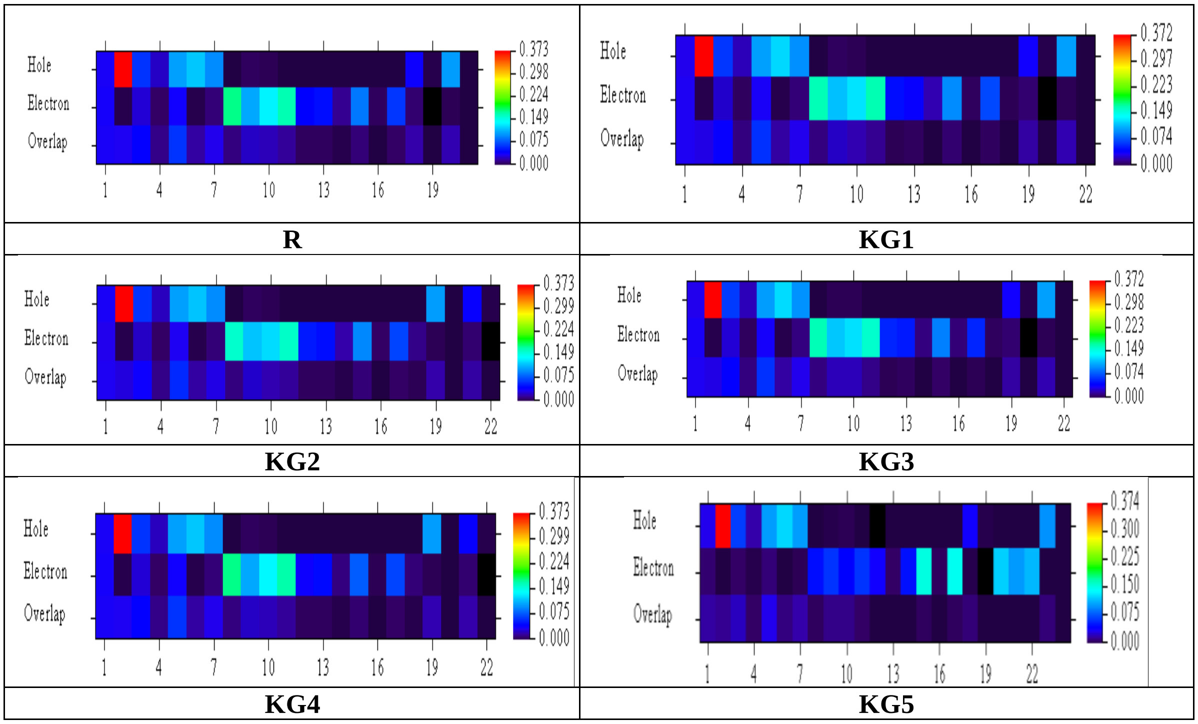

R **KG1**

KG2 **KG3**

KG4 **KG5**

Fig. 10: Presenting overlapping graphs of electrons and holes for all synthesized molecules.

Table 7: Glide molecular docking data of co-crystallized ligand, reference and top hit compound with an anti-inflammatory human target protein 4COX under investigation.

					4COX (Antiinflammatory)	
Ligand	**DScore (kcal/mol)**	**GScore (kcal/mol)**	**Glide Emodel**	**H-bond with Distance in Å**	**Polar interactions**	**Hydrophobic Interactions**
(A)Co-crystallized ligand	**-10.972**	**-10.973**	**-93.304**	**ARG120 (1.98) TYR355 (1.91) SER530 (2.13)**	**HIS90 SER353 SER530**	**VAL116, TYR348, VAL349, LEU352, TYR355, LEU359, PHE381, LEU384, TYR385, TRP387, PHE518, MET522, VAL523, ALA527, LEU531**
(B) FKB	**-8.087**	**-8.165**	**-57.491**	**-**	**HIS90 SER353 SER530**	**VAL116, VAL349, LEU352, TYR35, LEU359, PHE381, LEU384, TYR385, TRP387, PHE518, MET522, VAL523, ALA527, LEU531, LEU534**
(C) KG2	**-8.775**	**-8.853**	**-66.247**	**-**	**HIS90 SER353 SER530**	**MET113, VAL116, TYR348, VAL349, LEU352, TYR355, LEU359, PHE381, LEU384, TYR385, TRP387, PHE518, MET522, VAL523, ALA527, LEU531**

Glide Molecular Docking Results

The docking results of anti-inflammatory target protein 4COX with different ligands under investigation are given in Table-7 **(**provided in supplementary material). The co-crystallized ligand (Fig. 11.) interacts with the target protein via hydrogen bonding along with respective distances as ARG120 (1.98 Å), TYR355 (1.91 Å), and SER530 (2.13 Å). Several hydrophobic interactions are observed with VAL116, TYR348, VAL349, LEU352, TYR355, LEU359, PHE381, LEU384, TYR385, TRP387, PHE518, MET522, VAL523, ALA527, and LEU531. The hydrophobic interactions involve non-polar amino acid residues and thus facilitate the ligand's binding affinity. The G-Score is -10.973 kcal/mol. The FKB (reference compound) (Fig. 12.) does not engage in hydrogen bonding. However, it involves the hydrophobic interactions with VAL116, VAL349, LEU352, TYR35, LEU359, PHE381, LEU384, TYR385, TRP387, PHE518, MET522, VAL523, ALA527, LEU531, and LEU534. These interactions are responsible for stabilizing the ligand within the binding pocket of a target protein. The GScore is -8.165 kcal/mol, which shows the favorable binding energy of the complex. KG2 (Fig. 13.) interacts hydrophobically with MET113, VAL116, TYR348, VAL349, LEU352, TYR355, LEU359, PHE381, LEU384, TYR385, TRP387, PHE518, MET522, VAL523, ALA527, and LEU531 resulting in a G-Score of -8.853 kcal/mol. In addition, hydrogen bond formation is not observed. All the ligands mentioned above show polar interactions with HIS90, SER353, and SER530.

Table-8: Glide molecular docking data of co-crystallized ligand, reference and top hit compound with an anti-cancer human target protein 2WNQ under investigation.

				2WNQ (Anticancer)		
Ligand	**DScore (kcal/mol)**	**GScore (kcal/mol)**	**Glide Emodel**	**H-bond with Distance in Å**	**Polar interactions**	**Hydrophobic Interactions**
(1)Co-crystallized ligand	**-6.327**	**-7.024**	**-86.533**	**ALA114 (1.92, 2.00) ASP115 (1.83) ILE40 (2.37) ASP179 (1.88, 2.76) ALA165 (1.88)**	**ASN166**	**ILE40, VAL48, ALA61, ILE95, LEU111, LEU113, ALA114, ALA116, ALA165, PHE168**
(2) FKB	**-4.609**	**-4.686**	**-44.506**	**ALA114 (2.23), ASP179 (2.14)**	**-**	**ILE40, VAL48, ALA61, ILE95, LEU111, LEU113, ALA114, PHE168**
(3)KG4	**-4.959**	**-5.036**	**-44.912**	**ALA114 (2.15), ASP179 (2.10)**	**-**	**ILE40, VAL48, ALA61, ILE95, LEU111, LEU113, ALA114, PHE168**

Table-8 represents the docking scores and interactions between various prepared ligands and the anticancer target protein (PDB ID: 2WNQ) given in supplementary material. This table highlights insights into how these ligands interact with the protein and their potential anticancer characteristics. The co-crystallized ligand of the chosen anticancer target protein (Fig. 14.) interacts through hydrophobic interactions with ILE40, VAL48, ALA61, ILE95, LEU111, LEU113, ALA114, ALA116, ALA165, and PHE168. The G-Score of -7.024 kcal/mol. ALA114 (1.92 Å, 2.00 Å), ASP115 (1.83 Å), ILE40 (2.37 Å), ALA165 (1.88 Å), and ASP179 (1.88 Å, 2.76 Å) are the amino acid residues that are involved in hydrogen bonding. At the same time, the ASN166 is the only polar amino acid residue engaged in the polar interactions.The FKB (Fig. 15.) on interaction with 2WNQ (anticancer) protein showed the hydrophobic interactions with ILE40, VAL48, ALA61, ILE95, LEU111, LEU113, ALA114, and PHE168. It shows hydrogen bonding with ALA114 (2.23 Å) and ASP179 (2.14 Å). The docking score of -4.686 kcal/mol reflects the moderate binding affinity of the reference compound to the anticancer target protein. Polar interactions are not observed. KG4 (Fig. 16.) interacts hydrophobically with ILE40, VAL48, ALA61, ILE95, LEU111, LEU113, ALA114, and PHE168. The Gscore of -5.036 kcal/mol indicates the robust binding of KG4 to the anticancer protein. It showed the hydrogen bonding with ALA114 (2.15 Å) and ASP179 (2.10 Å).

The docking result of an antioxidant target protein 5M8Q with various ligands under study is given in Table-9 (supplementary material). The co-crystallized ligand (Fig. 17.) interacts with the target protein through hydrogen bonding along with respective distance as ARG321 (2.11, 2.71 Å). The hydrophobic interactions are observed with PHE362, PRO371, ALA372, VAL373, and LEU382. The polar interactions are seen with ASN378 and SER374. The relative GScore is -6.211 kcal/mol. The FKB (reference compound) (Fig. 18.) engages in hydrogen bonding with GLY389 (1.70 Å), and the hydrophobic interactions involve PHE362, LEU382, VAL391, and PHE400. HIS377, ASN378, HIS381, GLN390, and SER394 are involved in polar interactions. The G-Score is -5.194 kcal/mol.

KG1 (Fig. 19.) interacts hydrophobically with PHE362, LEU382, VAL391, and PHE400, resulting in a G-Score of -6.287 kcal/mol. In addition, GLY389 (1.81 Å) is involved in hydrogen bond formation. The polar interactions are evident with HIS377, ASN378, HIS381, GLN390, and SER394.

Table-9: Glide molecular docking data of co-crystallized ligand, reference and top hit compound with an antioxidant human target protein 5M8Q under investigation.

				5M8Q (Antioxidant)		
Ligand	**Dscore (kcal/mol)**	**GScore (kcal/mol)**	**Glide Emodel**	**H-bond with Distance in Å**	**Polar interactions**	**Hydrophobic Interactions**
(a)Co-crystallized ligand	**-6.211**	**-6.211**	**-67.601**	**ARG321 (2.11, 2.71)**	**ASN378 SER374**	**PHE362, PRO371, ALA372, VAL373, LEU382**
(b) FKB	**-5.116**	**-5.194**	**-45.936**	**GLY389 (1.70)**	**HIS377 ASN378 HIS381 GLN390 SER394**	**PHE362, LEU382, VAL391, PHE400**
(c) KG1	**-6.210**	**-6.287**	**-49.389**	**GLY389 (1.81)**	**HIS377 ASN378 HIS381 GLN390 SER394**	**PHE362, LEU382, VAL391, PHE400**

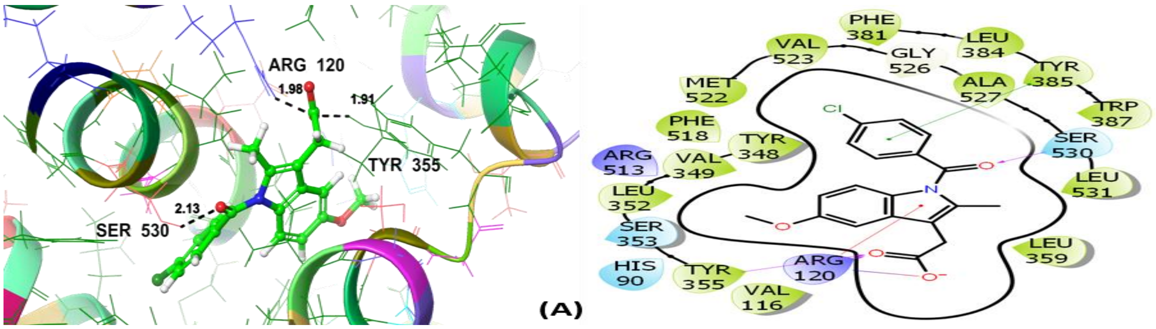

Fig. 11: Co-crystallized ligand (A)-3D and 2D interaction view with an anti-inflammatory target protein 4COX.

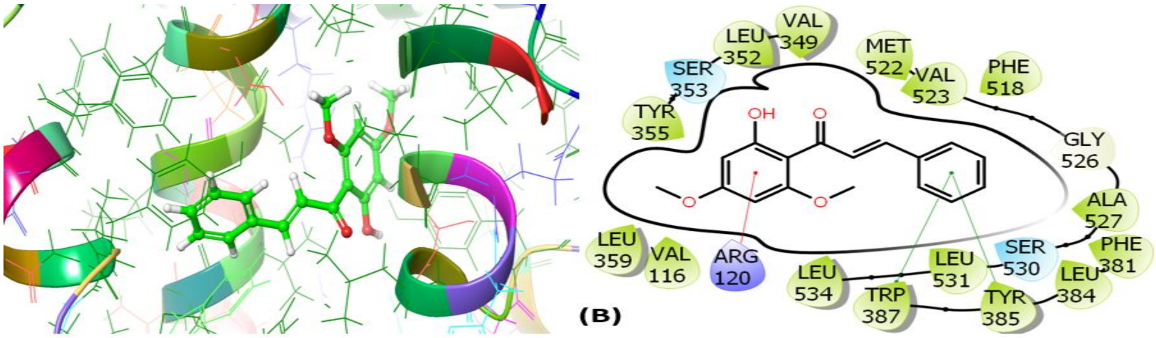

Fig. 12: FKB (B)-3D and 2D interaction view with an anti-inflammatory target protein 4COX.

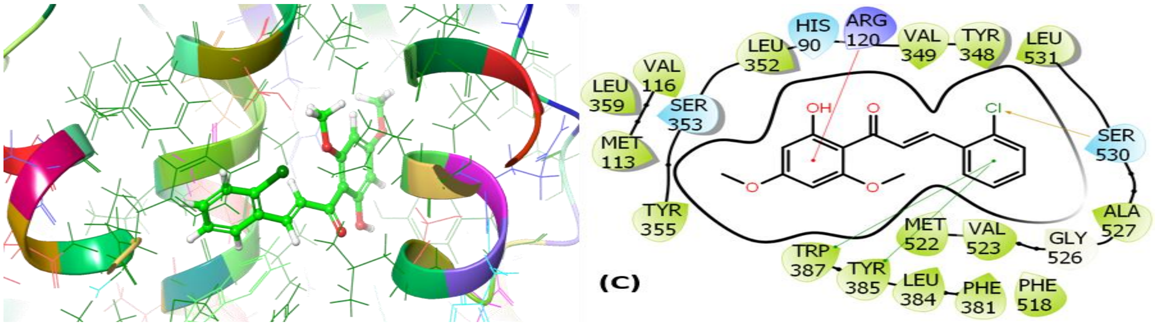

Fig. 13: KG2 (C)-3D and 2D interaction view with an anti-inflammatory target protein 4COX.

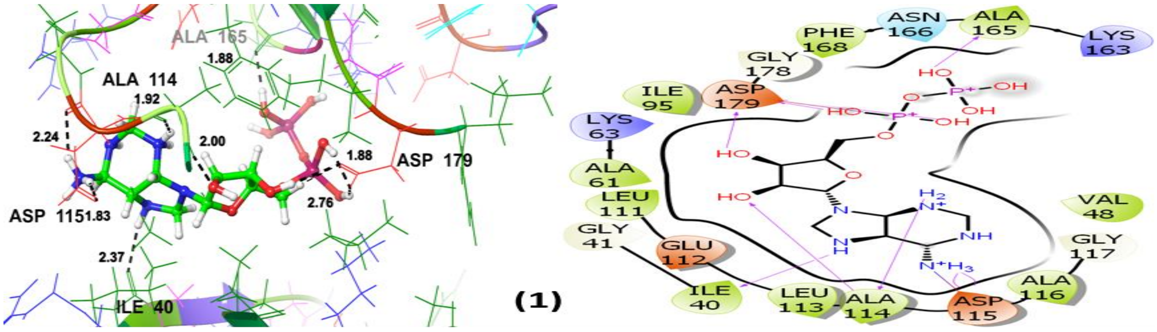

Fig. 14: Co-crystallized ligand (1)-3D and 2D interaction view with an anticancer target protein 2WNQ.

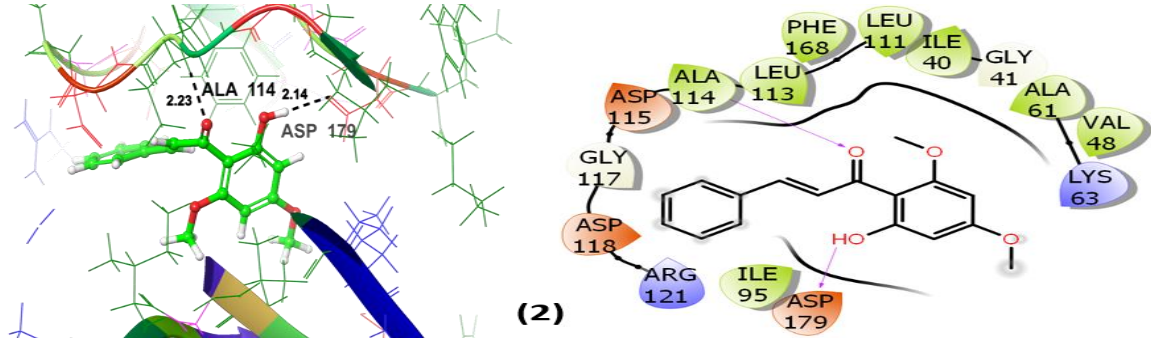

Fig. 15. FKB (2)-3D and 2D interaction view with an anticancer target protein 2WNQ.

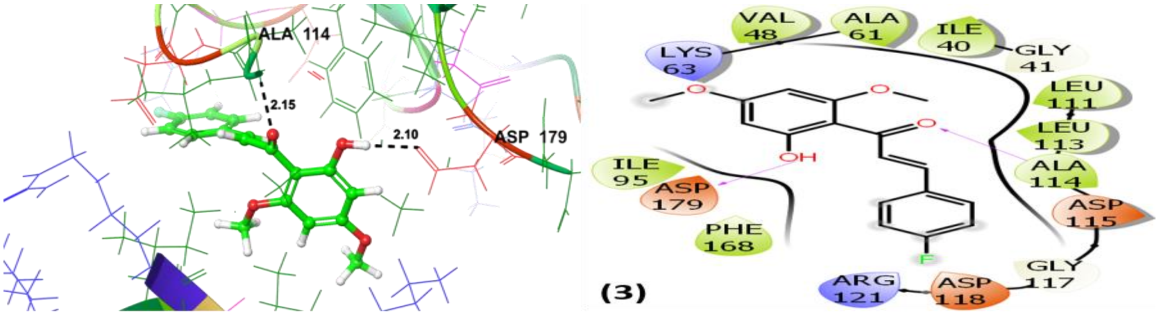

Fig. 16: KG4 (3)-3D and 2D interaction view with an anticancer target protein 2WNQ.

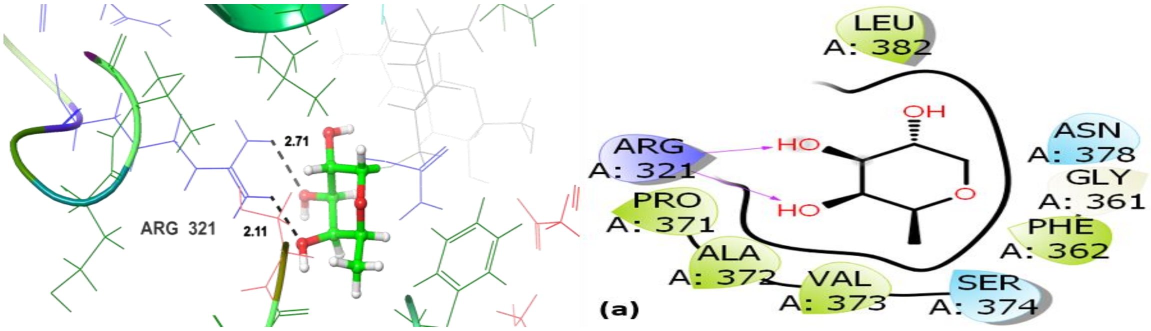

Fig. 17: Co-cryst ligand (a)-3D and 2D view with an antioxidant target protein 5M8Q.

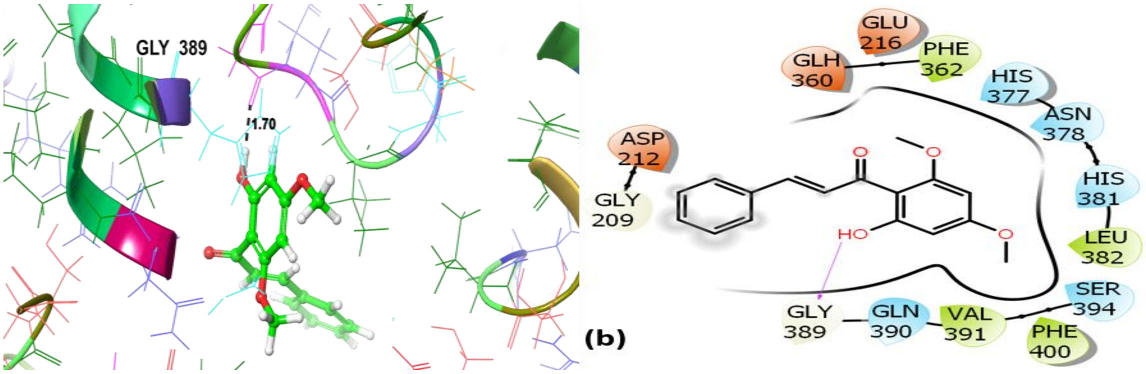

Fig. 18: FKB (b)-3D and 2D interaction view with an antioxidant target protein 5M8Q.

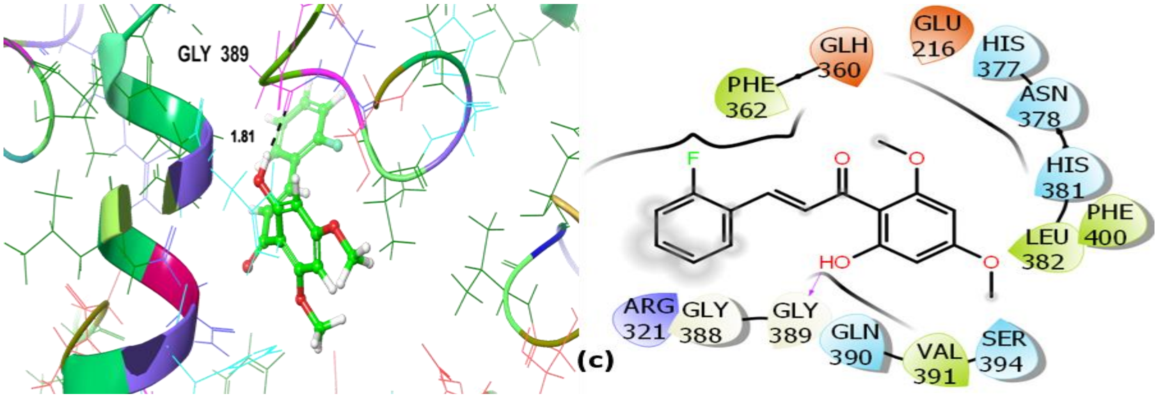

Fig. 19: KG1 (c)-3D and 2D interaction view with an antioxidant target protein 5M8Q.

The glide molecular docking study has thus established the following order of decreasing GScore values:

i. (4COX) Anti-inflammatory Order co-crystallized ligand (-10.973)> KG2 (-8.853) > KG1 (-8.851) > KG4 (-8.663) > FKB (-8.165) > KG5 (-8.008) > KG3 > (-7.906)
ii. (2WQN) Anti-cancer Order co-crystallized (-7.024) > KG4 (-5.036) > KG5 (-4.852) FKB (-4.686) > KG2 (-4.634) > KG1 (-4.602) > KG3 (-4.011)
iii. (5M8Q) Antioxidant Order KG1 (-6.287) > co-crystallized ligand (-6.211) > KG4 (-5.878) > KG5 (-5.222) > FKB (-5.194) > KG3 (-5.041) KG2 (-4.992).

Conclusion

Various advanced quantum molecular techniques were applied to evaluate the optoelectronic properties of KG1 to KG5. In this study, FKB showed D-A-π-A type morphology. The results indicated that all compounds exhibited a bathochromic shift in the UV absorption spectra leading towards higher efficiency. Due to extensive conjugation and the presence of the nitro group on KG5 showed the lowest excitation of 3.05 eV and reddish absorption spectra at 406 nm and a lower bandgap of 3.43 eV. KG5 has a lower E_b value than R, around 0.38 eV. Based on these results, the KG5 molecule was found to be the best molecule having excellent optoelectronic properties. The lower the value of the GScore in Glide molecular docking indicated the potency of a molecule. All the molecules exhibited several biological activities. Thus, the computational and molecular docking studies of KG2, KG4, and KG1 and related compounds indicated their potency.

Acknowledgment

One of us (Muhammad Nadeem Akhtar) is thankful to The Higher Education Commission (HEC) for the award of grant of NRPU grant No. 15788.

References

1. H. R. W. Dharmaratne, N. D. Nanayakkara, and I. A. Khan, Kavalactones from Piper methysticum, and their 13C NMR spectroscopic analyses. *Phytochem*; **59,** 429 (2002).
2. A. Abu Bakar, M. N. Akhtar, N. Mohd Ali, S. K. Yeap, C. K. Quah, W.-S. Loh, N. B. Alitheen, S. Zareen, Z. Ul-Haq, and S. a. A. Shah, Design, synthesis and docking studies of flavokawain B type chalcones and their cytotoxic effects on MCF-7 and MDA-MB-231 cell lines. *Molecules*; 616 (2018).
3. N. Abu, W. Y. Ho, S. K. Yeap, M. N. Akhtar, M. P. Abdullah, A. R. Omar, and N. B. Alitheen, The flavokawains: uprising medicinal chalcones. *Cancer Cell International;* **13**, 1 (2013).
4. N. a. A. Bakar, M. R. Sulaiman, N. Lajis, M. N. Akhtar, and A. S. Mohamad, Evaluation of Antinociceptive Profile of Chalcone Derivative (3-(2, 5-dimethoxyphenyl)-1-(5-methylfuran-2-yl) prop-2-en-1-one (DMPF-1) in vivo. *Journal of pharmacy & bioallied sciences*; **12,** S711 (2020).
5. K. Awasthi, N. Mishra, B. Kumar, M. Sharma, A. Bhattacharya, L. C. Mishra, and V. K. Bhasin, Potent antimalarial activity of newly synthesized substituted chalcone analogs in vitro. *Med. Chem*; **18**: (2009).
6. R. H. Hans, E. M. Guantai, C. Lategan, P. J. Smith, B. Wan, S. G. Franzblau, J. Gut, P. J. Rosenthal, and K. Chibale, Synthesis, antimalarial and antitubercular activity of acetylenic chalcones. BMCL, **20** (2010).
7. C. Dyrager, M. Wickström, M. Fridén-Saxin, A. Friberg, K. Dahlén, E. A. Wallén, J. Gullbo, M. Grøtli, and K. Luthman, Inhibitors and promoters of

tubulin polymerization: synthesis and biological evaluation of chalcones and related dienones as potential anticancer agents. *Bioorg. Med. Chem*. **19**: (2011).

8. C. Echeverria, J. F. Santibañez, O. Donoso-Tauda, C. A. Escobar, and R. Ramirez-Tagle, Structural antitumoral activity relationships of synthetic chalcones. *Int. J. Mol. Sci;* **10** (2009).
9. A. Kamal, G. Ramakrishna, P. Raju, A. Viswanath, M. J. Ramaiah, G. Balakishan, and M. Pal-Bhadra, Synthesis and anti-cancer activity of chalcone linked imidazolones. BMCL, **20**: (2010).
10. Y. H. Wang, H. H. Dong, F. Zhao, J. Wang, F. Yan, Y. Y. Jiang, and Y. S. Jin, The synthesis and synergistic antifungal effects of chalcones against drug resistant Candida albicans. BMCL, **26**: (2016).
11. T. N. Doan and D. T. Tran, Synthesis, antioxidant and antimicrobial activities of a novel series of chalcones, pyrazolic chalcones, and allylic chalcones. *JPP*; **2**: (2011).
12. S. Shenvi, K. Kumar, K. S. Hatti, K. Rijesh, L. Diwakar, and G. C. Reddy, Synthesis, anticancer and antioxidant activities of 2, 4, 5-trimethoxy chalcones and analogues from asaronaldehyde: Structure–activity relationship. *Eur J Med Chem;* **62**, (2013).
13. B. P. Bandgar, S. S. Gawande, R. G. Bodade, J. V. Totre, and C. N. Khobragade, Synthesis and biological evaluation of simple methoxylated chalcones as anticancer, anti-inflammatory and antioxidant agents. *Bioorganic & medicinal chemistry*; **18** (2010).
14. F. Herencia, M. P. Lo, A. Ubeda, and M. L. Ferrándiz, Nitric oxide-scavenging properties of some chalcone derivatives. Nitric oxide; **6**: (2002).
15. X. W. Zhang, D. H. Zhao, Y. C. Quan, L. P. Sun, X. M. Yin, and L. P. Guan, Synthesis and evaluation of antiinflammatory activity of substituted chalcone derivatives. *Med. Chem*; **19**: (2010).
16. M. N. Kamaldin, M. N. Akhtar, A. S. Mohamad, N. Lajis, E. K. Perimal, A. Akira, L. Ming-Tatt, D. A. Israf, and M. R. Sulaiman, Peripheral antinociception of a chalcone, flavokawin B and possible involvement of the nitric oxide/cyclic guanosine monophosphate/potassium channels pathway. *Molecules*, **18**: (2013).
17. A. S. Mohamad, M. N. Akhtar, S. I. Khalivulla, E. K. Perimal, M. H. Khalid, H. M. Ong, S. Zareen, A. Akira, D. A. Israf, and N. Lajis, Possible participation of nitric oxide/cyclic guanosine monophosphate/protein kinase C/ATP-sensitive K+ channels pathway in the systemic antinociception of Flavokawin B. BCPT; **108**: (2011).
18. N. Abu, M. N. Akhtar, S. K. Yeap, K. L. Lim, W. Y. Ho, A. J. Zulfadli, A. R. Omar, M. R. Sulaiman, M. P. Abdullah, and N. B. Alitheen, Flavokawain A induces apoptosis in MCF-7 and MDA-MB231 and inhibits the metastatic process in vitro. PLoS One; **9,** e105244 (2014).
19. N. Abu, N. Elyani Mohamed, S. Keong Yeap, K. Lam Lim, M. Nadeem Akhtar, A. Jamil Zulfadli, B. Boon Kee, M. Puad Abdullah, A. Rahman Omar, and N. Banu Alitheen, In vivo anti-tumor effects of flavokawain A in 4T1 breast cancer cell-challenged mice, *Anti-Cancer Agents in Medicinal Chemistry (Formerly Current Medicinal Chemistry-Anti-Cancer Agents);* **15**: (2015).
20. G. Trucks, H. Schlegel, G. Scuseria, M. Robb, J. Cheeseman, G. Scalmani, V. Barone, B. Mennucci, G. Petersson, and H. Nakatsuji, *Gaussian*. Inc., Wallingford CT: (2009).
21. R. Dennington, T. Keith, and J. Millam, *GaussView 5.0, Gaussian*. Inc., Wallingford; **20**: (2008).
22. S. Khan, R. Hussain, A. Satar, M. A. Assiri, M. Imran, A. Hussain, M. A. Yawer, M. Y. Mehboob, S. Hussain, and M. Khalid, Quantum chemical designing of novel fullerene-free acceptor molecules for organic solar cell applications. *J. Mol. Model;* **28**, (2022).
23. J. G. Moberly, M. T. Bernards, and K. V. Waynant, *Key features and updates for origin 2018*. Journal of cheminformatics; **10**: (2018).
24. R. Hussain, M. U. Khan, M. Y. Mehboob, M. Khalid, J. Iqbal, K. Ayub, M. Adnan, M. Ahmed, K. Atiq, and K. Mahmood, *Enhancement in photovoltaic properties of N, N-diethylaniline based donor materials by bridging core modifications for efficient solar cells*. ChemistrySelect; **5**: (2020).
25. S. Tang and J. Zhang, *Design of donors with broad absorption regions and suitable frontier molecular orbitals to match typical acceptors via substitution on oligo (thienylenevinylene) toward solar cells*. J. Comput. Chem; **33** (2012).
26. M. T. El Sayed, M. a. S. El-Sharief, E. S. Zarie, N. M. Morsy, A. R. Elsheakh, A. Voronkov, V. Berishvili, and G. S. Hassan, *Design, synthesis, anti-inflammatory activity and molecular docking of potential novel antipyrine and pyrazolone analogs as cyclooxygenase enzyme (COX) inhibitors*. BMCL; **28**: (2018).
27. M. Aziz, S. A. Ejaz, N. Tamam, F. Siddique, N. Riaz, F. A. Qais, S. Chtita, and J. Iqbal,*Identification of potent inhibitors of NEK7 protein using a comprehensive computational approach*. Scientific reports; **12**: (2022).
28. N. Ramzan, M. Azeem, K. Mahmood, S. Shah, F. R. S. Chughtai, M. Hanif, N. Ameer, Z. Bashir, F. Siddique, and M. Qaisar,*Cellular and Non-cellular Antioxidant Properties of Vitamin E–Loaded Metallic-Quercetin/Polycaprolactone*

Nanoparticles for the Treatment of Melanogenesis. AAPS PharmSciTech; **24**: (2023).

P. W. Rose, B. Beran, C. Bi, W. F. Bluhm, D. Dimitropoulos, D. S. Goodsell, A. Prlić, M. Quesada, G. B. Quinn, and J. D. Westbrook, *The RCSB Protein Data Bank: redesigned web site and web services*. Nucleic acids research; **39**: (2010).

29. S. Roy, R. Sharma, and A. Kumar,*17 Molecular Docking and Molecular Dynamics in Signal Analysis*. Signal Analysis in Pharmacovigilance: Principles and Processes: 210 (2024).
30. C. Lu, C. Wu, D. Ghoreishi, W. Chen, L. Wang, W. Damm, G. A. Ross, M. K. Dahlgren, E. Russell, and C. D. Von Bargen, *OPLS4:* Improving force field accuracy on challenging regimes of chemical space. *JCTCCE*; **17**: (2021).
31. B. L. Jejurikar and S. H. Rohane, Drug designing in discovery studio. (2021).
32. J. Ekowati, N. W. Diyah, B. A. Tejo, and S. Ahmed, Chemoinformatics approach to design and develop vanillin analogs as COX-1 inhibitor. Journal of public health in Africa; **14** (2023).

R. A. Friesner, R. B. Murphy, M. P. Repasky, L. L. Frye, J. R. Greenwood, T. A. Halgren, P. C. Sanschagrin, and D. T. Mainz, Extra precision glide*:* Docking and scoring incorporating a model of hydrophobic enclosure for protein− ligand complexes. Journal of medicinal chemistry; **49** (2006).

33. B. Civalleri, C. M. Zicovich-Wilson, L. Valenzano, and P. Ugliengo, B3LYP augmented with an empirical dispersion term (B3LYP-D*) as applied to molecular crystals. CrystEngComm; **10** (2008).
34. J.-D. Chai and M. Head-Gordon, Long-range corrected hybrid density functionals with damped atom–atom dispersion corrections. Physical Chemistry Chemical Physics; **10** (2008).
35. T. Yanai, D. P. Tew, and N. C. Handy, A new hybrid exchange–correlation functional using the Coulomb-attenuating method (CAM-B3LYP). Chemical physics letters; **393** (2004).
36. C. Adamo and V. Barone, Exchange functionals with improved long-range behavior and adiabatic connection methods without adjustable parameters: The m PW and m PW1PW models. *J. Chem. Phys*; **108** (1998).
37. N. Mica, S. a. J. Almahmoud, L. K. Jagadamma, G. Cooke, and I. D. W. Samuel, An investigation of the role acceptor side chains play in the processibility and efficiency of organic solar cells fabricated from small molecular donors featuring 3, 4-ethylenedioxythiophene cores. *RSC advances*; **8** (2018).
38. M. U. Khan, M. Khalid, M. Ibrahim, A. a. C. Braga, M. Safdar, A. A. Al-Saadi, and M. R. S. A. Janjua, First theoretical framework of triphenylamine–dicyanovinylene-based nonlinear optical dyes: structural modification of π-linkers. *J. Phys. Chem. C* **122** (2018).
39. M. R. S. A. Janjua, M. U. Khan, B. Bashir, M. A. Iqbal, Y. Song, S. a. R. Naqvi, and Z. A. Khan, Effect of π-conjugation spacer (CC) on the first hyperpolarizabilities of polymeric chain containing polyoxometalate cluster as a side-chain pendant: A DFT study. Computational and Theoretical Chemistry; **994**: 34-40 (2012).
40. M. U. Khan, M. Ibrahim, M. Khalid, S. Jamil, A. A. Al-Saadi, and M. R. S. A. Janjua,Quantum chemical designing of indolo [3, 2, 1-jk] carbazole-based dyes for highly efficient nonlinear optical properties. *Phys. Lett* **719**: (2019).
41. M. U. Khan, M. Ibrahim, M. Khalid, A. a. C. Braga, S. Ahmed, and A. Sultan, Prediction of second-order nonlinear optical properties of D–π–A compounds containing novel fluorene derivatives: a promising route to giant hyperpolarizabilities. *J. Clust. Sci*.; **30** (2019).
42. N. Ohta, K. Yamashita, and A. Muraoka, Mechanism of charge transfer and separation in polymer/nonfullerene acceptor organic solar cells. *Bulletin of the American Physical Society*; **65**: (2020).
43. A. Lagunin, A. Stepanchikova, D. Filimonov, and V. Poroikov, *PASS:* prediction of activity spectra for biologically active substances. *J. Bioinform*; **16**(8): (2000).
44. R. U. Janicke, M. L. Sprengart, M. R. Wati, and A. G. Porter, Caspase-3 is required for DNA fragmentation and morphological changes associated with apoptosis. *JBC*; **273** (1998).
45. V. Arkhipov, P. Heremans, E. Emelianova, and H. Baessler, Effect of doping on the density-of-states distribution and carrier hopping in disordered organic semiconductors. *Phys. Rev* B; **71** (2005).
46. B. Hartenstein and H. Bässler, Transport energy for hopping in a Gaussian density of states distribution. *J. Non-Cryst. Solids*; **190** (1995).
47. M. Y. Mehboob, R. Hussain, M. M. A. Iqbal, Z. Irshad, and M. Adnan, First principle theoretical designing of W-shaped Dithienosilole-based acceptor materials having efficient photovoltaic properties for high-performance organic solar cells. *J. Phys. Chem. Solids*; **157**: (2021).
48. M. Y. Mehboob, M. Adnan, R. Hussain, A. Farhad, and Z. Irshad,Butterfly-shaped hole transport materials with outstanding photovoltaic properties for organic solar cells. *Opt. Quantum Electron*; **53** (2021).
49. M. Y. Mehboob, R. Hussain, Z. Irshad, and M. Adnan, Role of acceptor guests in tuning optoelectronic properties of benzothiadiazole core based non-fullerene acceptors for high-performance

bulk-heterojunction organic solar cells. *J. Mol. Model*; **27**(8): 1-16 (2021).

50. P. Politzer and J. S. Murray, An overview of strengths and directionalities of noncovalent interactions: σ-holes and π-holes. Crystals; **9** (2019).
51. M. Y. Mehboob, F. Hussain, R. Hussain, S. Ali, Z. Irshad, M. Adnan, and K. Ayub, Designing of Inorganic Al12N12 Nanocluster with Fe, Co, Ni, Cu and Zn Metals for Efficient Hydrogen Storage Materials. *J COMPUT BIOPHYS CHE;* **20** (2021).
52. F. Younas, M. Y. Mehboob, K. Ayub, R. Hussain, A. Umar, M. U. Khan, Z. Irshad, and M. Adnan, Efficient Cu decorated inorganic B12P12 nanoclusters for sensing toxic COCl2 gas: a detailed DFT study. *J COMPUT BIOPHYS CHE*; **20** (2021).
53. M. Y. Mehboob, R. Hussain, M. Adnan, and Z. Irshad, End-capped molecular engineering of S-shaped hepta-ring-containing fullerene-free acceptor molecules with remarkable photovoltaic characteristics for highly efficient organic solar cells. *Energy Technol*; **9** (2021).
54. M. Y. Mehboob, R. Hussain, M. U. Khan, M. Adnan, A. Umar, M. U. Alvi, M. Ahmed, M. Khalid, J. Iqbal, and M. N. Akhtar, Designing N-phenylaniline-triazol configured donor materials with promising optoelectronic properties for high-efficiency solar cells. *Comput. Theor. Chem*; **1186**: (2020).
55. M. Y. Mehboob, R. Hussain, Z. Irshad, and M. Adnan,Enhancement in the photovoltaic properties of hole transport materials by end-capped donor modifications for solar cell applications. *Bull. Korean Chem. Soc*; **42** (2021).
56. M. Y. Mehboob, M. Adnan, R. Hussain, and Z. Irshad, Quantum chemical designing of banana-shaped acceptor materials with outstanding photovoltaic properties for high-performance non-fullerene organic solar cells. *Synthetic Metals*; **277**: (2021).
57. M. Y. Mehboob, M. U. Khan, R. Hussain, K. Ayub, A. Sattar, M. K. Ahmad, Z. Irshad, and M. Adnan, Designing of benzodithiophene core-based small molecular acceptors for efficient non-fullerene organic solar cells. Spectrochimica Acta Part A: Molecular and Biomolecular Spectroscopy; **244**: (2021).
58. C. Liu, L. Liu, N. Qiu, X. Wan, C. Li, and Y. Lu, A novel chlorinated small molecule donor for efficient binary and ternary all-small-molecule organic solar cells. *Org. Electron*; **106**: (2022).
59. M. Y. Mehboob, M. U. Khan, R. Hussain, M. Khalid, J. Yaqoob, R. Rehman, M. B. A. Siddique, M. M. Alam, M. Imran, and K. Ayub, First example of vinylbenzene based small photovoltaic molecules: Towards the development of efficient D-π-A configured optoelectronic materials for bulk heterojunction solar cells. *Phys. Rev. B Condens*; **633**: (2022).
60. 62. M. M. A. Iqbal, M. Y. Mehboob, T. Hassan, M. S. Khan, and M. Arshad, High electron mobility due to extra π-conjugation in the end-capped units of non-fullerene acceptor molecules: a DFT/TD-DFT-based prediction. *J. Mol. Model*; **28** (2022).
61. M. Ans, J. Iqbal, Z. Ahmad, S. Muhammad, R. Hussain, B. Eliasson, and K. Ayub, Designing three-dimensional (3D) non-fullerene small molecule acceptors with efficient photovoltaic parameters. ChemistrySelect; **3** (2018).
62. Y. Li and C. Ullrich, Time-dependent transition density matrix. *Chemical Physics*; **391** (2011).
63. P. Å. Malmqvist,Calculation of transition density matrices by nonunitary orbital transformations. *Int. J. Quantum Chem*; **30** (1986).
64. S. Hussain, R. Hussain, M. Y. Mehboob, S. a. S. Chatha, A. I. Hussain, A. Umar, M. U. Khan, M. Ahmed, M. Adnan, and K. Ayub, Adsorption of phosgene gas on pristine and copper-decorated B12N12 nanocages: a comparative DFT study. *ACS omega;* **5** (2020).
65. A. Dkhissi, Excitons in organic semiconductors. *Synthetic metals*; **161** (2011).
66. S. Hussain, S. A. Shahid Chatha, A. I. Hussain, R. Hussain, M. Y. Mehboob, T. Gulzar, A. Mansha, N. Shahzad, and K. Ayub, Designing novel Zn-decorated inorganic B12P12 nanoclusters with promising electronic properties: a step forward toward efficient CO2 sensing materials. *ACS omega;* **5** (2020).
67. N. Liang, K. Sun, Z. Zheng, H. Yao, G. Gao, X. Meng, Z. Wang, W. Ma, and J. Hou,Perylene diimide trimers based bulk heterojunction organic solar cells with efficiency over 7%. *Adv. Energy Mater.* **6**: (2016).
68. S. Hussain, S. a. S. Chatha, A. I. Hussain, R. Hussain, M. Y. Mehboob, S. Muhammad, Z. Ahmad, and K. Ayub, Zinc-doped boron phosphide nanocluster as efficient sensor for SO2. *J. Chem.* **2020**: (2020).